Enhanced Electronic Transport in Fe^{3+}-doped TiO_2 for High Efficiency Perovskite Solar Cells

Xiangling Gu,[a] Yafei Wang,[a] Ting Zhang,[a] Detao Liu,[a] Rui Zhang,[a] Peng Zhang,[a] Jiang Wu,[c] Zhi David Chen,*[ab] and Shibin Li *[a]

[a]School of Optoelectronic Information, State Key Laboratory of Electronic Thin Films and Integrated Devices, University of Electronic Science and Technology of China (UESTC), Chengdu, 610054, China

[b]Department of Electrical & Computer Engineering and Center for Nanoscale Science & Engineering, University of Kentucky, Lexington, Kentucky 40506, USA

[c]Department of Electronic and Electrical Engineering, University College London, Torrington Place, London WC1E 7JE,United Kingdom

Abstract

Oxygen vacancies in non-stoichiometric TiO_2 electron transport layer can capture injected electrons and act as recombination centers. In this study, the compact TiO_2 electron transport layer of perovskite solar cells (PSCs) is doped with different molar ratios of Fe^{3+} in order to passivate such defects and improve its electron transport property. The electrical conductivity, absorption, crystal structure, and the performance of the PSCs are systematically studied. It shows that Fe^{3+}-doping improves the conductivity of TiO_2 compact layer compared with the pristine TiO_2, boosting the photovoltaic performance of PSCs. The reduced trap-filled limit voltage (V_{TFL}) of the Fe^{3+}-doped TiO_2 compact layer suggests that trap density in the Fe^{3+}-TiO_2 film is much lower than that of a pristine TiO_2 film. With the optimized doping concentration (1 mol%) of Fe^{3+}, the best power conversion efficiency of PSCs is improved from 16.02% to 18.60%.

Keywords: Fe^{3+}-doped TiO_2, electronic transport, perovskite solar cells, oxygen vacancies, conductivity

1. Introduction

The past several years have witnessed the fast development of a brand-new type of solar cell based on organic-inorganic halide perovskite materials.[1,2] The power conversion efficiency (PCE) of perovskite solar cells (PSCs) has rapidly increased from 3.8% to 22.1% since it was first reported in 2009.[3-8] For PSCs, the electron transport layer (ETL) plays a significant role in transporting electrons and blocking holes. In the vast majority of PSCs, TiO_2 is the preferred material for ETL because of its superior electronic properties.[9-12] For example, the conduction band of TiO_2 matches well with that of the perovskite active layer. Meanwhile, TiO_2 is low-cost, compatible with various deposition methods, chemically stable and highly conductive.[12-17] However, there exist oxygen vacancies, Ti interstitial sites, and trap states in TiO_2 ETL, which can capture injected electrons and act as recombination centers. As a result, these defects and trap states dramatically degrade the efficiency and stability of devices.[18-21] Therefore, fabrication of a TiO_2 ETL with reduced oxygen vacancies and defects is critical to improve the charge extraction and collection of PSCs.

Previous works have demonstrated that it can effectively enhance electron transport in the TiO_2 by doping suitable metal ions. In 2014, Snaith's group doped Al into a TiO_2 compact layer and found that the conductivity of TiO_2 compact layer was increased by several orders of magnitude due to reduced oxygen vacancies in the TiO_2 ETL.[20] Zhou *et al.* reported that yttrium-doped TiO_2 compact layer improved the conductivity and carrier extraction ability of the ETL, and enhanced the cell's PCE to

19.3%.[22] In addition, Zn-doped, Nb-doped, Mg-doped and Li-doped TiO_2 ETLs have also been reported.[23-28] However, very limited study has been reported on Fe-doped TiO_2 ETL for perovskite solar cells. Previous studies of Fe-doped TiO_2 were devoted to improving photocatalytic property, visible light activity or tuning the band-gap structure of TiO_2 rather than enhancing its electrical properties for application in PSCs.[29-31] For example, Yalcin *et al.* found that visible light activity and photocatalytic property of TiO_2 particles were improved by Fe^{3+}-doping and the same result was reported by Zhu *et al.*[29,32] Fe^{3+} has the same valence as Al^{3+} and Y^{3+} and similar radius to Ti^{4+} (Fe^{3+} =0.064nm, Ti^{4+}=0.068nm).[33] Therefore, Fe^{3+} cations can penetrate into the TiO_2 lattice and substitute Ti cations.[29] One would expect that Fe^{3+}-doped TiO_2 ETLs could lead to further improved photovoltaic performance of PSCs compared with other doped ETLs.

In this work, we doped a TiO_2 compact layer with Fe^{3+} ions (Fe^{3+}-TiO_2) and used it as ETL for perovskite solar cells. The Fe^{3+}-doped TiO_2 precursor solution can be obtained easily through mixing $Fe(NO_3)_3$ solution with TiO_2 solution in proper proportion, including 0.5 mol%, 1 mol%, 2 mol%, and 5 mol%. As a result of Fe^{3+} doping, we demonstrate that the conductivity increases significantly by an order of magnitude and the trap-filled limit voltage (V_{TFL}) of the Fe^{3+}-doped TiO_2 compact layer obviously decreases compared with the pure TiO_2 compact layer.[34] Consequently, we obtain a high efficiency of 18.01% for $MAPbI_3$-based solar cells and 18.6% for $Cs_{0.05}(MA_{0.17}FA_{0.83})_{0.95}Pb(I_{0.83}Br_{0.17})_3$-based cells. The results reported in this work demonstrate the performance of PSCs can be enhanced by doping TiO_2 compact layer

with Fe^{3+} ions.

2. Results and discussion

As shown in Fig. 1a, the mesoporous-structure perovskite solar cells, consisting of FTO/ Fe^{3+}-TiO_2 (or TiO_2)/ meso-TiO_2/ $MAPbI_3$/ Spiro-OMeTAD/ Au, are fabricated. Fig. 1b and c are the scanning electron microscopy (SEM) images of the pristine TiO_2 and 1 mol% Fe^{3+}-TiO_2 layers. The results show that both the Fe^{3+}-TiO_2 and pure TiO_2 compact layers are uniform and homogeneous. The SEM cross-sectional image of a PSC in Fig. 1d shows that perovskite thin films with large crystalline grains are prepared. Fig. 1e exhibits that the color of the Fe^{3+}-TiO_2 solution gradually changes to red with the increase of doping concentration. In order to investigate the distribution of Fe elements, we measured energy dispersive spectrometer (EDS) spectra at five separated positions for the 5 mol% Fe^{3+}-TiO_2 film (≈700 nm). As displayed in Fig. S1, S2 and Table 1, the atomic ratios of Fe/Ti at five positions show a small difference, and the obtained average atomic ratio in EDS analysis is 6.4%. The EDS result confirms that Fe element is homogeneously distributed within TiO_2 film.

X-ray diffraction (XRD) measurement is conducted to elucidate the lattice structure. As shown in Fig. 2a, all the TiO_2 compact layers doped with different doping concentrations are anatase phase. This is because the ionic radius of Fe^{3+} is very similar to Ti^{4+}, and the Fe^{3+} dopants cannot change the lattice parameter of TiO_2. In Fig. 2b, the absorption of Fe^{3+}-TiO_2 compact films shows enhanced visible light activity or red shift. The absorbance increases with the increase of Fe^{3+} doping

concentration. This has been attributed to the formation of a Fe-dopant energy level within the band gap of TiO_2.[29,31,32,35] XRD patterns of $MAPbI_3$ thin films on doped and undoped TiO_2 compact layers shown in Fig. 2c reveal an identical crystalline structure as reported in the previous literature.[36] The absorption shown in Fig. 2d imply that Fe^{3+}-doping of TiO_2 compact layer indicates negligible effects on the absorption of $MAPbI_3$ thin films in the range of visible light.

The current density versus voltage (J-V) curves shown in Fig. 3a reveal that the PSCs doped with 1 mol% Fe^{3+} yield the best performance. As shown in Fig. 3b, it is known that oxygen vacancies or Ti interstitials are the predominant non-stoichiometry defects in TiO_2 lattice, resulting in the conversion of Ti^{4+} to Ti^{3+}.[37-40] Therefore, Ti^{3+} defects can induce a shallow energy level below the conduction band and act as electron trap sites, which can capture electrons and reduce electron transport efficiency and conductivity of TiO_2. Based on above analysis and previous literatures, as shown in Fig. 3c, two Fe^{3+} can substitute two Ti^{3+} adjacent to an oxygen defect. Consequently, this substitution effectively passivates or removes oxygen vacancy defects or traps in TiO_2 compact layer. The Fe^{3+}-doping mechanism is consistent with that of the Al-doped TiO_2. This conclusion is supported by the increased conductivity and decreased trap-filled limit voltage (V_{TFL}) of TiO_2 compact layer thin film in the following study.

To explore the role of Fe^{3+}-doping, X-ray photoelectron spectroscopy (XPS) measurement was carried out. Fig. 3d shows the XPS spectra of the Fe^{3+}-doped and undoped TiO_2 samples. The binding energies in the range 710.4-712.3 eV and

724.0-724.5 eV should be assigned to $2p_{3/2}$ and $2p_{1/2}$ of Fe^{3+} cations.[35,41] The signal of Fe $2p_{3/2}$ (1 mol% Fe^{3+}-TiO_2) is weak due to the low doping level, but still obvious compared with the pristine TiO_2. The result indicates that Fe elements doped into the TiO_2 lattice are in a trivalent valence state. The atomic ratios of Fe/Ti for pristine and Fe^{3+}-doped TiO_2 are shown in Table 2 and the survey XPS spectra is presented in Fig. S3. In Fig. 3e, the binding energy of O 1s peak centered at 529.13 eV and 529.19 eV can be ascribed to TiO_2. The smaller peak at 531.02 eV and 531.21 eV may be assigned to the surface hydroxyl groups or chemisorbed water molecules.[32] The slightly higher O 1s binding energy for the Fe^{3+}-doped sample further suggests the linkage of Fe-O-Ti bond in Fe^{3+}-TiO_2. Ti $2p_{3/2}$ and Ti $2p_{1/2}$ peaks for all samples in Fig. 3f are located at binding energies of 457.96 eV and 463.63 eV, respectively. Perhaps, due to the low concentration of Fe^{3+}, the shift of Ti 2p peaks is below the detection limit.

It is demonstrated that the transport of photogenerated electrons in films is limited by space-charge effects.[34] The density of free carriers is reduced when the trap centers capture the photogenerated free carriers, leading to a smaller current with a small slope at low bias voltage. However, as the voltage is continuously increased, all the traps are filled. The current quickly increases nonlinearly with a higher slope if the bias voltage exceeds the kink point. The kink point is the trap-filled limit voltage (V_{TFL}). So we can estimate the values of V_{TFL} by calculating the intersection of the two slopes. Furthermore, V_{TFL} can be determined by the trap-state density (N_t).

$$V_{TFL} = \frac{eN_t d^2}{2\varepsilon\varepsilon_0} \quad (1)$$

Where e is the elementary charge of the electron, d and ε are the thickness and relative dielectric constant of the active layer, ε_0 is the vacuum permittivity.[42] According to equation (1), we can see that V_{TFL} increases with the increase of trap density.

To confirm whether doping Fe^{3+} can effectively reduce the trap density in the TiO_2 compact layer, we measured the log-log plot of I-V curves for Fe^{3+}-doped and undoped devices with a structure shown in the inset of Fig. 4a. The nonlinear curve in Fig. 4a indicates the existence of space charges, e.g. Ti interstitials, oxygen vacancies, etc. For the best Fe^{3+}-doping condition, the I-V curve is more linear. The V_{TFL} of 1 mol% Fe^{3+}-TiO_2 is estimated to be 0.45 V, which is pretty lower than that of pure TiO_2 (0.64 V) and Fig. 4a shows a significant difference in current between doped and pristine samples. The result demonstrates that the trap-state density in the Fe^{3+}-TiO_2 film is much lower than that in a pristine TiO_2 film. The reason is possibly because Fe^{3+}-doping suppresses space charges and increases the carrier density and conductivity of TiO_2. These can be verified from the results of the Hall Effect measurement. The conductivity versus dopant concentration curves and results of Hall Effect are shown in the inset of Fig. 4a and Table S1. Table S1 shows that the conductivity of Fe^{3+}-doped TiO_2 is increased by an order of magnitude compared with pristine TiO_2, which is possibly caused by the increased carrier density and reduced trap states in ETL.

Fig. 4b is the hysteresis curve for the cells. Under the best doping concentration of Fe^{3+}, a high PCE of 18.01% from reverse scan and 17.22% from forward scan for

$CH_3NH_3PbI_3$-based cells is obtained. We observed a slight reduction in hysteresis compared with the undoped devices. This may be attributed to Fe^{3+} ions passivating the electronic defects or trap states caused by non-stoichiometric oxygen-induced defects within the TiO_2 lattice. The passitvation enhanced the extraction of free electrons and suppressed the cell's hysteresis.[19,20] Fig. 4c shows a steady-state current density of 20.15 mA/cm^2 and efficiency of 17.12% after 150 s operation at a bias voltage of 0.83 V from reverse scan direction for the Fe^{3+}-TiO_2/ $MAPbI_3$-based cell, whereas the TiO_2-based control cell displays a steady-state current density of 16.24 mA/cm^2 and efficiency of 14.13% at a bias voltage of 0.77 V. Fig. 4d shows that the external quantum efficiency (EQE) of the Fe^{3+}-doped device is much higher than the undoped one. The highest value for Fe^{3+}-doped device is almost 91%, which is mainly due to enhanced electron extraction via using Fe^{3+}-TiO_2. The integrated Jsc for Fe^{3+}-doped and undoped device in Fig. 4d is 22.06 mA/cm^2 and 20.19 mA/cm^2, respectively. According to Table 3, the PSCs with 1 mol% Fe^{3+}-TiO_2 compact layer exhibit the best performance. The V_{oc}, J_{sc} and FF increase from 1.02 V to 1.06 V, from 22.03 mA/cm^2 to 23.22 mA/cm^2, and from 63.25% to 66.68% (mean values with reverse scan). As a result, the average PCE is raised from 14.59% to 17.01%.

Electrochemical impedance spectroscopy (EIS) is utilized to investigate the charge-transport process and carrier recombination of the TiO_2-based perovskite cells. The inset in Fig. 4e is an equivalent circuit of the cells and our test frequency is from 1Hz to 1MHz under 1 sun illumination. The parameters of carrier transport and recombination in PSCs are fitted by analyzing Nyquist curves. Normally, there are

two arcs on the Nyquist curve, where the first arc at high frequency is related to the transport and extraction in the cathode and the second arc is related to the recombination process between different layers.[43-45] Nyquist plot in Fig. 4e and parameters in Table S2 show that recombination resistance of Fe^{3+}-TiO_2-based cells at interfaces between different films is significantly larger than TiO_2-based cells. Since a larger recombination resistance indicates a lower recombination loss, this result illustrates that the recombination process is effectively suppressed for Fe^{3+}-TiO_2-based cells. It further manifests that the Fe^{3+}-TiO_2 has fewer trapping centers and improved interface properties (more information about Nyquist plot can be obtained from Electronic Supplementary Information (ESI)).

Furthermore, to determine the junction property of the cell, a model based on the single heterojunction solar cell is adopted.[46] In a heterojunction solar cell, the value of the ideality factor (N) represents the quality of a junction and the carrier recombination mechanisms. The smaller value of N, the less recombination caused by defect in the cell. Calculation method of N can be found in ESI and Fig. S4 is the box plot of N at different doping concentrations. In our experiment, we calculated N for doped and undoped samples under light conditions shown in Fig. 4f and Table 3 , and the mean values of 1 mol% Fe^{3+}-TiO_2 and pure TiO_2 perovskite cells are 2.95 and 3.99, respectively. We can see that the former is much smaller than the latter, which probably means that the carrier recombination in Fe^{3+}-TiO_2 cells is reduced due to the reduction of trap states in the doped TiO_2 compact layer.

Fig. 5a-d are the statistics of Voc, FF, Jsc, and PCE of 100 devices based on

different doping conditions. The statistical distributions of $V_{oc,}$ J_{sc}, FF and PCE for the TiO_2 and Fe^{3+}-TiO_2 based cells in Fig. 5 show that 1mol% Fe^{3+} -doped cells exhibit higher photovoltaic parameters compared with the others. Thus, photovoltaic performance of the cells can be effectively improved by doping Fe^{3+} in the ETL. The stability of $MAPbI_3$-based cells tested for three weeks in the dark is provided, as shown in Fig. S5 and S6. The devices were exposed directly to the air without encapsulation (25%-35% relative humidity (RH), 25℃). It has been demonstrated that the degradation of PSCs is mainly ascribed to the decomposition of perovskite in air.[47] As shown in Fig. S5, the perovskite solar cells based on Fe^{3+}-doped and pristine TiO_2 exhibited similar performance deterioration.

We also fabricated Cs/FA/MA-based PSCs with Fe^{3+}-doped compact layer as reported by Saliba.[48] In Fig. S7a, the device yields a high PCE of 18.60% from reverse scan and 17.88% from forward scan under best doping concentration, whereas the TiO_2-based control devices exhibited a PCE of 16.02% and 14.86% respectively. In addition, Fig. S7b shows a steady-state current density of 20.75 mA/cm^2 and efficiency of 17.6% for Fe^{3+}-doped Cs/FA/MA-based cell after 150 s operation from reverse scan direction at the bias voltage of 0.84 V. The results demonstrate that the high performance Fe^{3+}-TiO_2-based PSCs is repeatable. Detailed parameters of the devices are presented in the inset table of Fig. S7a.

3. Conclusions

In summary, we fabricated $MAPbI_3$-based and Cs/FA/MA-based perovskite solar cells by doping compact TiO_2 layer with different Fe^{3+} concentrations. Due to the

reduction of electron trap density, the Fe^{3+}-doped TiO_2 compact layer shows enhanced conductivity and reduced V_{TFL}. Therefore, Fe^{3+}-doped compact TiO_2 films extract photogenerated electrons more efficiently. As a result, cells with doped ETLs are successfully improved compared with cells with pristine TiO_2. Finally, the PCE is improved from 14.59% to 18.01% for $MAPbI_3$-based cell, while the PCE of Cs/FA/MA-based cell is increased from 16.02% to 18.6%. So Fe^{3+} doped TiO_2 compact layer provides a feasible way to fabricate high performance PSCs.

Notes

The authors declare no competing financial interest.

Acknowledgements

This work was supported by National Natural Science Foundation of China under Grant Nos. 61421002, 61574029, 61471085, and 61371046. This work was also partially supported by University of Kentucky.

REFERENCES

1 M. A. Green, A. Ho-Baillie and H. J. Snaith, *Nat. Photonics*, 2014, **8**, 506-514.

2 D. Zheng, G.Yang, Y. Zheng, P. Fan, R. Ji, J. Huang and J. Yu, *Electrochim. Acta*, 2017, **247**, 548-557.

3 A. Kojima, K. Teshima, Y. Shirai and T. Miyasaka, *J. Am. Chem. Soc.*, 2009, **131** 6050-6051.

4 Y. Wang, S. Li, P. Zhang, D. Liu, X. Gu, H. Sarvari and Z. D. Chen, *Nanoscale*, 2016, **8**, 19654-19661.

5 Y. Zhao and K. Zhu, *J. Am. Chem. Soc.*, 2014, **136**, 12241-12244.

6 D. Zheng, W. Huang, P. Fan, Y. Zheng, J. Huang and J. Yu, *ACS Appl. Mater. Interfaces*, 2017, **9**, 4898-4907.

7 W. S. Yang, B. W. Park, E. H. Jung, N. J. Jeon, Y. C. Kim, D. U. Lee and S. I. Seok, *Science*, 2017, **356**, 1376-1379.

8 Y. Zhao, and K. Zhu, *Chem. Soc. Rev.*, 2016, **45**, 655-689.

9 W. S. Yang, J. H. Noh, N. J. Jeon, Y. C. Kim, S. Ryu, J. Seo and S. I. Seok, *Science*, 2015, **348**, 1234-1237.

10 D. Bi, W. Tress, M. I. Dar, P. Gao, J. Luo, C. Renevier and J. D. Decoppet, *Sci. Adv.*, 2016, **2**, e1501170.

11 N. Ahn, D. Y. Son, I. H. Jang, S. M. Kang, M. Choi and N. G. Park, *J. Am. Chem. Soc.*, 2015, **137**, 8696-8699.

12 S. Li, P. Zhang, H. Chen, Y. Wang, D. Liu, J. Wu and Z. D. Chen, *J. Power Sources*, 2017, **342**, 990-997.

13 M. M. Lee, J. Teuscher, T. Miyasaka, T. N. Murakami and H. J. Snaith, *Science*, 2012, **338**, 643-647.

14 X. Li, D. Bi, C. Yi, J. D. Décoppet, J. Luo, S. M. Zakeeruddin and M. Grätzel, *Science*, 2016, **353**, 58-62.

15 J. Burschka, N. Pellet, S. J. Moon, R. Humphry-Baker, P. Gao, M. K. Nazeeruddin and M. Grätzel, *Nature*, 2013, **499**, 316-319.

16 T. Zhu and S. P. Gao, *J. Phys. Chem. C*, 2014, **118**, 11385-11396.

17 H. Yu, S. Zhang, H. Zhao, G. Will and P. Liu, *Electrochim. Acta*, 2009, **54**, 1319-1324.

18 H. S. Kim, C. R. Lee, J. H. Im, K. B. Lee, T. Moehl, A. Marchioro, S. J. Moon, R. Humphry-Baker, J. H. Yum, J. E. Moser, M. Grätzel and N. G. Park, *Sci. Rep.*, 2012, **2**, 591.

19 F. Giordano, A. Abate, J. P. Correa Baena, M. Saliba, T. Matsui, S. H. Im, S. M. Zakeeruddin, M. K. Nazeeruddin, A. Hagfeldt and M. Graetzel, *Nat. Commun.*, 2016, **7**, 10379.

20 S. K. Pathak, A. Abate, P. Ruckdeschel, B. Roose, K. C. Gödel, Y. Vaynzof and A. Sepe, *Adv. Funct. Mater.*, 2014, **24**, 6046-6055.

21 C. O'Rourke and D. R. Bowler, *J. Phys. Chem. C*, 2014, **118**, 7261-7271.

22 H. Zhou, Q. Chen, G. Li, S. Luo, T. B Song, H. S. Duan, Z. Hong, J. You, Y. Liu

and Y. Yang, *Science*, 2014, **345**, 542-546.

23 D. Liu, S. Li, P. Zhang, Y. Wang, R. Zhang, H. Sarvari and Z. D. Chen, *Nano Energy*, 2017, **31**, 462-468.

24 M. Lv, W. Lv, X. Fang, P. Sun, B. Lin, S. Zhang, X. Xu, J. Ding and N. Yuan, *RSC Adv.*, 2016, **6**, 35044-35050.

25 M. Yang, R. Guo, K. Kadel, Y. Liu, K. O'Shea, R. Bone, X. Wang, J. He and W. Li, *J. Mater. Chem. A*, 2014, **2**, 19616-19622.

26 J. Wang, M. Qin, H. Tao, W. Ke, Z. Chen, J. Wan, P. Qin, L. Xiong, H. Lei, H. Yu and G. Fang, *Appl. Phys. Lett.*, 2015, **106**, 121104.

27 X. Yin, Y. Guo, Z. Xue, P. Xu, M. He and B. Liu, *Nano Res.* 2015, **8**, 1997-2003.

28 X. Yin, Z. Xu, Y. Guo, P. Xu and M. He, *ACS Appl. Mater. Interfaces*, 2016, **8**, 29580-29587.

29 Y. Yalçın, M. Kılıç and Z. Çınar, *Appl. Catal., B*, 2010, **99**, 469-477.

30 W. Y. Teoh, R. Amal, L. Mädler and S. E. Pratsinis, *Catal. Today*, 2007, **120**, 203-213.

31 S. George, S. Pokhrel, Z. Ji, B. L. Henderson, T. Xia, L. Li and L. Mädler, *J. Am. Chem. Soc*., 2011, **133**, 11270-11278.

32 J. Zhu, F. Chen, J. Zhang, H. Chen and M. Anpo, *J. Photochem. Photobiol., A*, 2006, **180**, 196-204.

33 T. A. Egerton, E. Harris, E. J. Lawson, B. Mile and C. C. Rowlands, *Phys. Chem. Chem. Phys.*, 2001, **3**, 497-504.

34 R. H. Bube, *J. Appl. Phys.*, 1962, **33**, 1733-1737.

35 V. N. Nguyen, N. K. T. Nguyen and P. H. Nguyen, *Adv. Nat. Sci.: Nanosci. Nanotechnol.*, 2011, **2**, 035014.

36 Q. Dong, Y. Yuan, Y. Shao, Y. Fang, Q. Wang and J. Huang, *Energy Environ. Sci.*, 2015, **8**, 2464-2470.

37 A. K. Ghosh, F. G. Wakim, R. R. Addiss Jr, *Phys. Rev.*, 1969, **184**, 979.

38 M. A. Henderson, *Surf. Sci.*, 1999, **419**, 174-187.

39 M. Nolan, S. D. Elliott, J. S. Mulley, R. A. Bennett, M. Basham and P. Mulheran,

Phys. Rev. B, 2008, **77**, 235424.

40 S. Wendt, P. T. Sprunger, E. Lira, G. K. Madsen, Z. Li, J. Ø. Hansen and F. Besenbacher, *Science*, 2008, **320**, 1755-1759.

41 C. D. Wagner, W. M. Riggs, L. E. Davis, J. F. Moulder and G. E. Muilenberg, Handbook of X-Ray Photoelectron Spectroscopy. *Perkin-Elmer Corp., Physical Electronics Division, USA*, 1979, chapter **2**, page 42 (O), page 68 (Ti), page 76 (Fe).

42 J. H. Heo, M. S. You, M. H. Chang, W. Yin, T. K. Ahn, S. J. Lee and S. H. Im, *Nano Energy*, 2015, **15**, 530-539.

43 G. Veerappan, D. W. Jung, J. Kwon, J. M. Choi, N. Heo, G. R. Yi and J. H. Park, *Langmuir*, 2014, **30**, 3010-3018.

44 V. Gonzalez-Pedro, E. J. Juarez-Perez, W. S. Arsyad, E. M. Barea, F. Fabregat-Santiago, I. Mora-Sero and J. Bisquert, *Nano Lett.*, 2014, **14**, 888-893.

45 A. Dualeh, T. Moehl, N. Tétreault, J. Teuscher, P. Gao, M. K. Nazeeruddin, M. Grätzel, *Acs Nano*, 2013, **8**, 362-373.

46 J. Shi, J. Dong, S. Lv, Y. Xu, L. Zhu, J. Xiao and Q. Meng, *Appl. Phys. Lett.*, 2014, **104**, 063901.

47 G. Niu, W. Li, F. Meng, L. Wang, H. Dong and Y. Qiu, *J. Mater. Chem. A*, 2014, **2**, 705-710.

48 M. Saliba, T. Matsui, J. Y. Seo, K. Domanski, J. P. Correa-Baena, M. K. Nazeeruddin and M. Grätzel, *Energy Environ. Sci.*, 2016, **9**, 1989-1997.

Figures and tables:

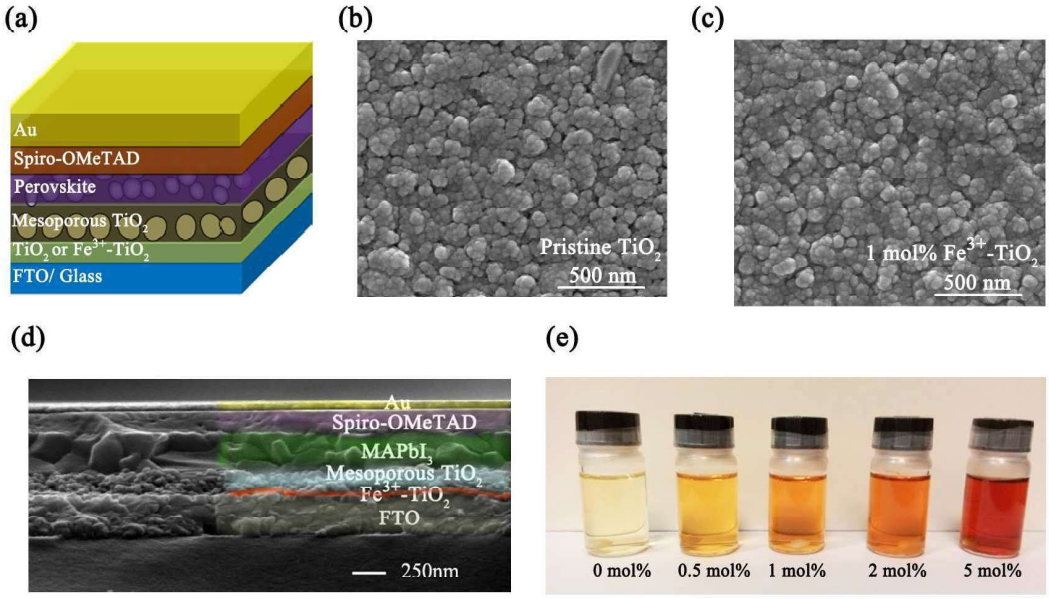

Fig. 1 (a) Schematic diagram of mesoporous $MAPbI_3$-based solar cell. (b) SEM image of FTO/ TiO_2. (c) SEM image of FTO/ 1 mol% Fe^{3+}-TiO_2. (d) Cross-sectional SEM image of the cell with a structure: FTO/ Fe^{3+}-TiO_2/ meso-TiO_2/ $MAPbI_3$/ Spiro-OMeTAD/ Au. (e) Solutions of pristine TiO_2 and Fe^{3+}-TiO_2.

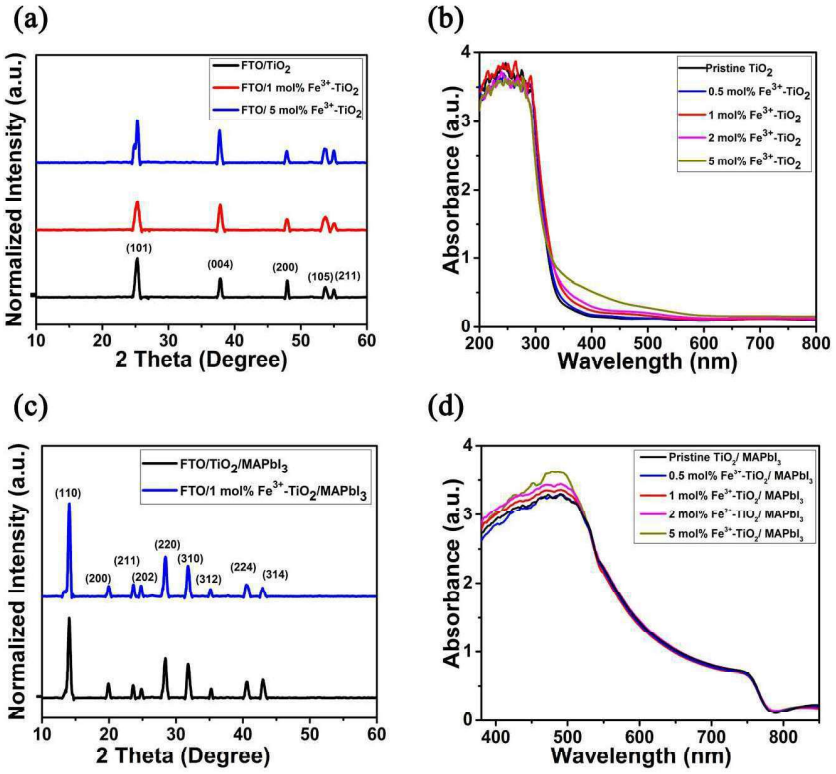

Fig. 2 (a) XRD pattern of pristine TiO_2 and Fe^{3+}-TiO_2. (b) The UV-vis absorption curves of the pristine TiO_2 or Fe^{3+}-TiO_2 compact layer. (c) XRD patterns of $MAPbI_3$ thin films with doped and pure TiO_2 compact layer.(d) Absorption lines of the cells with the following structure: FTO/ TiO_2 or Fe^{3+}-TiO_2/ $MAPbI_3$.

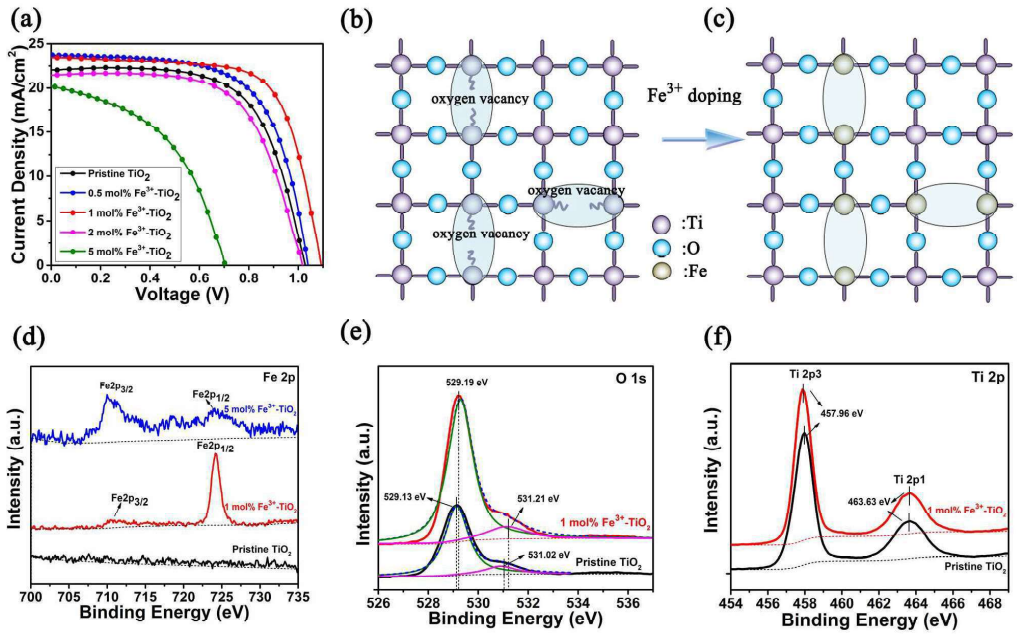

Fig. 3 (a) J-V curves of the TiO_2-based and Fe^{3+}-TiO_2-based $MAPbI_3$ solar cells. (b) Defects in the pristine TiO_2. (c) Fe^{3+} substitution at the Ti^{3+} sites passivates oxygen vacancy defects. (d) XPS spectra of pristine TiO_2 and Fe^{3+}-TiO_2. (e) XPS spectra of O 1s peaks for pristine TiO_2 and 1 mol% Fe^{3+}-TiO_2 samples. (f) XPS spectra of Ti 2p peaks.

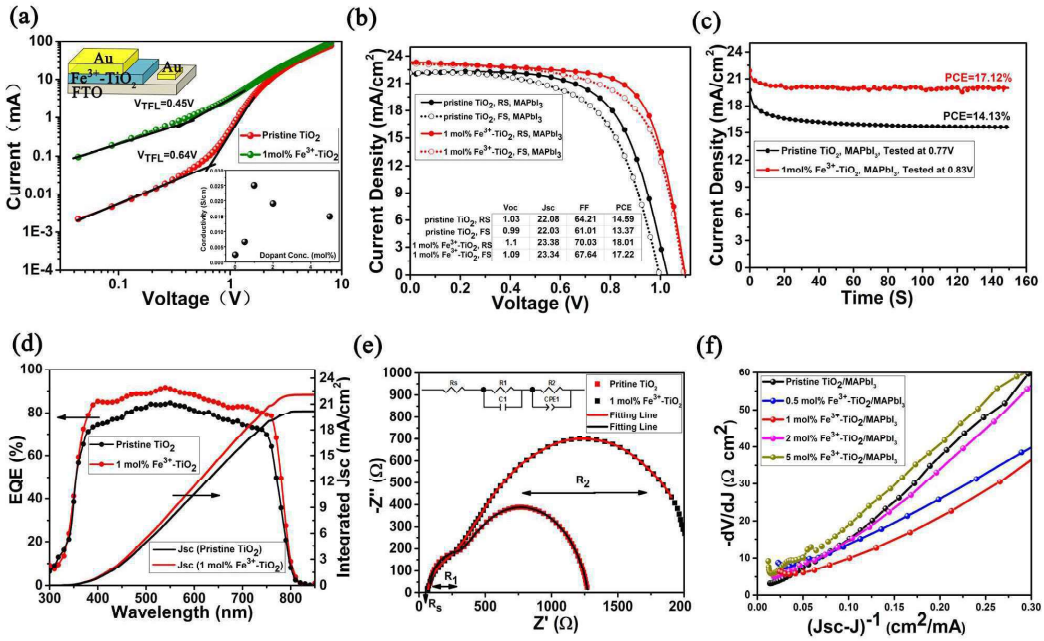

Fig. 4 (a) Log-log plot of I-V curves of Fe^{3+}-TiO_2 and TiO_2 devices with the structure of FTO/ Fe^{3+}-TiO_2 (or TiO_2) /Au. (b) J-V curves of the FTO/ 1 mol% Fe^{3+}-TiO_2 (or TiO_2)/ meso-TiO_2/ $MAPbI_3$/ Spiro-OMeTAD/ Au cells. (c) Steady-state current density of the Fe^{3+}-TiO_2-based and TiO_2-based cells. (d) EQE curves and integrated current density of Fe^{3+}-TiO_2-based and TiO_2-based $MAPbI_3$ cells. (e) Nyquist plot of the $MAPbI_3$-based cells with the following structure: FTO/ TiO_2 or Fe^{3+}-TiO_2/ meso-TiO_2/ $MAPbI_3$/ Spiro-OMeTAD/ Au. (f) -dV/dJ vs $(Jsc-J)^{-1}$ curves in the approximately linear region of the PSCs.

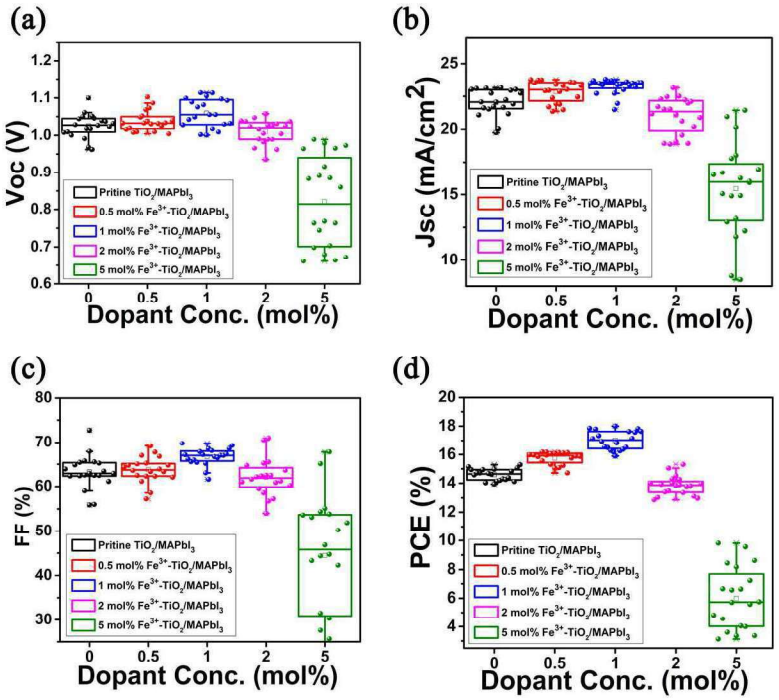

Fig. 5 The photovoltaic parameters' statistical distribution of the $MAPbI_3$-based PSCs with different Fe^{3+}-doping concentrations. (a) Distribution of Voc. (b) Distribution of Jsc. (c) Distribution of FF. (d) Distribution of PCE.

Table 1 The ratios of Fe/Ti in 5 mol% Fe^{3+}-doped compact TiO_2 film measured by EDS analysis.

position	Fe/Ti (%)
1	5.9
2	5.7
3	6.5
4	7.1
5	6.8
Average	6.4

Table 2 The theoretical and experimental atomic ratios of Fe/Ti for pristine and Fe^{3+}-doped TiO_2.

	Fe/Ti (%)	
Sample	Theoretical value	XPS analysis
Pristine TiO_2	0	0
1mol%-Fe^{3+}-TiO_2	1	1.37
5 mol%-Fe^{3+}-TiO_2	5	6.41

Table 3 The parameters (mean value based on 100 Cells) of $MAPbI_3$ solar cells with different Fe^{3+}-doping concentrations in TiO_2 compact layer.

Sample	Voc (V)	Jsc (mA/cm^2)	FF (%)	N	PCE (%)
Pristine TiO_2	1.02	22.03	63.25	3.99	14.59
0.5 mol% Fe^{3+}-TiO_2	1.04	22.84	63.77	3.38	15.74
1 mol% Fe^{3+}-TiO_2	1.06	23.22	66.68	2.95	17.01
2 mol% Fe^{3+}-TiO_2	1.01	21.03	62.07	4.58	13.85
5 mol% Fe^{3+}-TiO_2	0.82	15.44	44.45	8.04	5.98